




An adaptive scheme for the efficient evaluation of integrals in two-dimensional boundary element method

R. Si Hadj Mohand*, , Y. Belkacemi and S. Rechak

Abstract

An efficient analysis with the boundary element method requires an accurate evaluation of all the boundary integrals. Typically, nonsingular integrals are solved numerically using Gauss quadrature. Therefore, the

*Corresponding author

Received 14 May 2025; revised 6 August 2025; accepted 17 August 2025

Rahim Si Hadj Mohand

Laboratory of Green Mechanics and Development (LGMD), Department of mechanical engineering, Ecole Nationale Polytechnique, Algiers, Algeria. e-mail: rahim.si_hadj_mohand@g.enp.edu.dz

Yacine Belkacemi

Laboratory of Green Mechanics and Development (LGMD), Department of mechanical engineering, Ecole Nationale Polytechnique, Algiers, Algeria. e-mail: yacine.belkacemi@g.enp.edu.dz

Said Rechak

Laboratory of Green Mechanics and Development (LGMD), Department of mechanical engineering, Ecole Nationale Polytechnique, Algiers, Algeria. e-mail: said.rechak@g.enp.edu.dz

How to cite this article

Si Hadj Mohand, R., Belkacemi, Y. and Rechak, S., An adaptive scheme for the efficient evaluation of integrals in two-dimensional boundary element method. *Iran. J. Numer. Anal. Optim.*, 2025; 15(4): 1420-1463. <https://doi.org/10.22067/ijnao.2025.93526.1647>

development of criteria and schemes that determine the appropriate Gauss order while maintaining a balance between accuracy and performance is of great importance.

In the present work, an adaptive integration criterion tailored for two-dimensional elasticity problems is introduced and verified. This criterion is formulated as an empirical formula, incorporating a parameter ranging from zero to unity. This parameter enables control over computational effort, making the criterion very efficient across a wide range of applications, from thick structures to extremely thin ones where near-singularities are pronounced.

The proposed integration criterion is tested on a very thin structure, where it showed a high degree of accuracy and effectiveness in solving problems with a very pronounced boundary layer effect. Additionally, the criterion demonstrated its advantage by reducing and moderating computational overhead in the case of pre-treatment of near-singularities by a semi-analytical technique or a variable transformation technique.

AMS subject classifications (2020): 74S15, 65R20, 65D30.

Keywords: Boundary integrals, Near-singularity, Gauss quadrature, Integration criterion, Thin structures.

1 Introduction

The accurate evaluation of boundary element integrals is of crucial importance in any boundary element method (BEM) analysis. The boundary integrals appearing in the BEM method involve kernel functions with terms of the form $\frac{1}{r^p}$ or $\log\left(\frac{1}{r}\right)$ with r the shortest distance between the source point and the boundary element. This nature causes a singular behavior when source points approach the boundary (r tends to zero). Thus, depending on the ratio $\lambda = \frac{r}{L}$ (with L the element length) integrals are classified into three major categories (Regular, Singular and Near-Singular), as schematized in Figure 1.

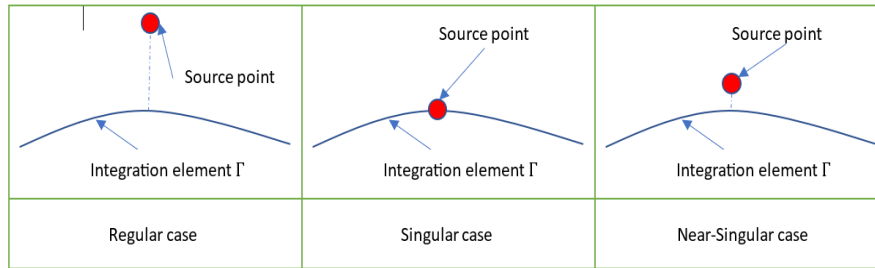


Figure 1: Boundary integral types

When the source point is sufficiently distant from the boundary element, the integral becomes regular. In this case, its numerical evaluation using Gauss quadrature with a relatively small order is sufficient. By contrast, when the source point coincides with the boundary element ($\lambda = 0$), the integral becomes singular. Several techniques have been proposed in the BEM literature to evaluate singular integrals, including analytical integration [32, 43, 44, 31, 47, 33], indirect methods [15, 17, 6, 7, 35], semi-analytical methods [16, 14, 37, 2], coordinate transformation [40, 20], and the use of singularity-reduced kernels [26]. Other methods directly formulate fundamental solutions, as in the novel scaled coordinate transformation BEM (SCTBEM [42, 19]), which converts the domain integral into a boundary integral, leading to the elimination of the low-order singularity.

The third type (near-singular integrals) arises when the source point is very close but not coinciding with the boundary element ($\lambda \approx 0$). While they are regular in nature and do not exhibit mathematical singularities, their evaluation is challenging due to steep variations of the integrand around the projection of the source point. This phenomenon is commonly known as the boundary layer effect, which arises in several applications of the BEM, such as thin-walled structures and thin coatings [3, 47, 37, 12, 46], crack-related problems [37, 5, 26, 30, 2, 33, 34], contact problems [8, 18], and near-boundary field calculations [6, 32, 13]. To deal with the boundary layer effect and near-singular integrations causing it, several techniques have been developed:

Element subdivision: A numerical technique proposed by Lachat and Watson [25], based on subdividing the original element into smaller subelements, thereby concentrating Gauss points around the projection of the source point.

Semi-analytical techniques: Methods such as singularity subtraction, proposed by Cruse and Aithal [9] and Mi and Aliabadi [28], are employed.

Variable transformation: This approach involves applying a nonlinear variable transformation that weakens the near-singular behavior and smooths the sharp peak of the integrand. Several transformations have been proposed, including the polynomial transformation of Telles [40], the optimal transformations of Sladek and Sladek [38], the distance transformation of Ma and Kamiya [27], and the sinh transformation of Johnston and Elliott [21], which was further extended by Gu et al. [12, 13] and Zhang, Gong, and Gao [45].

The use of Gauss quadrature is essential for most of the techniques cited above, either for evaluating the entire integral in numerical techniques or for evaluating the regular part and the transformed integral in semi-analytical techniques and variable transformations, respectively. Thus, determining the number of Gauss points for a given integral is of great importance. The set of rules and guidelines that determines the smallest order of quadrature guaranteeing a specified precision is called an integration criterion. The need to derive effective and precise criteria has led to several publications on this subject, where different integration criteria and upper-bound error formulas have been proposed.

The first work prior to any publications on this subject was the contribution of Stroud and Secrest [39], who proposed a formula for calculating the upper-bound error of Gaussian numerical integration. Based on this formula, Lachat and Watson [25] proposed the first integration criterion for functions of the form $\frac{1}{r^2}$, applicable to three-dimensional (3D) structures, which was further simplified by Mustoe [29] and Gao and Davies [11], who provided simpler approximate formulas for the upper-bound error estimate. Jun and Beer, [22] again used the upper-bound error formula of Stroud and Secrest [39] and proposed a new criterion for functions of the form $(\frac{1}{r^p}, p = 1, 2, 3)$, applicable in both (two-dimensional) 2D and 3D structures, presented in tabular format.

After performing an extensive numerical study on the error distribution around a flat rectangular 3D element, Bu and Davies [4] developed a new integration criterion for 3D problems. This criterion is presented both in tables and as empirical formulas and was further improved by Gao and Davies

[11], who proposed a unified approximation formula based on Bu and Davies' [4] numerical experiments.

Eberwien, Duencer, and Moser [10] followed a similar numerical strategy as Bu and Davies [4] and applied it in the 2D case by considering two reference elements, one flat and the other slightly curved. Unlike the research works cited above, the influence of the shape functions and the Jacobian was taken into consideration. Thus, the considered integrands are of the form

$$f(\xi) = (r(\xi))^p \times \Psi_m(\xi) \times J(\xi), \quad p = 1, 2.$$

The numerical study performed in [10] showed that the errors predicted by the previous publications [25, 39, 22, 4, 29, 11] were underestimated. This is due to the nonconsideration of the shape functions and the Jacobian. The criterion proposed by Eberwien, Duencer, and Moser was tested on a benchmark problem and showed a clear improvement in the results compared to its predecessors.

In 2020, Junhao, Zhipeng, and Yongqiang [23] accomplished an extensive numerical study on integrands of the form $(\frac{1}{r^p}, p = 1, 2, 3)$, and proposed a new upper-bound error estimate formula, which showed a certain gain in efficiency and precision compared to previous formulas. The gain in performance is especially visible at very small λ ratios.

In 2023, Zhou, Yang, and Chen [48] introduced a new adaptive scheme leveraging deep machine learning and AI technologies. Their approach categorizes the ratio λ into three distinct intervals, incorporates the sinh variable transformation for small values of λ , and predicts the required number of Gauss points using a trained neural network or its recorded data. This technique achieves a good level of precision, with significantly fewer Gauss points and reduced CPU time.

In the current study, a new integration criterion is introduced. It is formulated through empirical formulas, which determine the required number of Gauss points to attain one of three precision levels ($\epsilon = 10^{-2}, 10^{-3}, 10^{-4}$), depending on the λ ratio and the nature of the kernel. Specifically designed for 2D linear elasticity problems, this criterion was derived following an extensive numerical testing. Two bounding empirical formulas were established:

The lower-bound formulas is deduced by considering integrands of the form

$$f(\xi) = \frac{1}{r(\xi)^p}, \quad p = 1, 2,$$

while the upper-bound one by considering the complete form of the integrands as encountered in 2D-elasticity BEM

$$f(\xi) = F(P(\xi), P_0) \times \Psi_m(\xi) \times J(\xi),$$

where $F(P(\xi), P_0)$ represents one of the kernel functions of 2D-elasticity BEM, $P(\xi)$ and P_0 denote the field and source points, respectively, and $\Psi_m(\xi)$ and $J(\xi)$ denote the shape function and the Jacobian. Finally, a third formula is defined by the combination of the two bounding ones, using a real parameter $\alpha \in [0, 1]$, which allows control over the computational effort and facilitates its adjustment depending on application requirements.

Tested on an extremely thin structure, the new criterion demonstrated better and more stable precision compared to existing methods, even in regions of extreme thinness where the achieved relative error is lower than the target upper bound. The results highlight an underestimation of errors by existing criteria and error-bound formulas, due to the nonconsideration of the complete form of the kernels. Another advantage observed is a performance enhancement for moderate values of the λ ratio compared to the formulas outlined in [23]. These moderate values of λ commonly arise when employing the element subdivision technique, which is preferred in BEM applications over the use of high-order quadratures, since very high quadrature orders lead to floating-point round-off errors. Additionally, Gauss–Legendre abscissas and weights are not computed dynamically at runtime; instead, a limited set of predefined abscissas and corresponding weights is typically available and prescribed in the program.

Finally, the proposed criterion incorporates a parameter that can effectively reduce computational effort, especially in cases where integrands are treated using coordinate transformation or other semi-analytical techniques that mitigate or eliminate the near-singular behavior.

2 A brief review of the BEM for elasticity problems

Solving elasticity problems using the BEM is achieved by interpreting the partial differential equations that govern the problem in the form of integral equations.

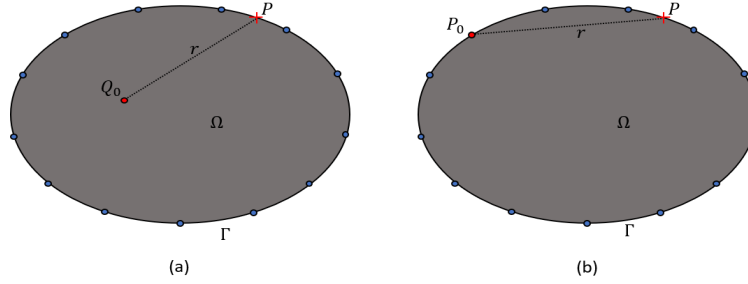


Figure 2: BEM Modeling of an elastic domain - (a) Source point inside the domain (b) source point on the boundary

Let us consider a linear elastic domain Ω with boundary $\Gamma = \partial\Omega$ (Figure 2). There are generally six integral equations that arise in any boundary element analysis. By neglecting the body forces, these equations are defined as [1, 6, 14]:

$$u_i(Q_0) = \int_{\Gamma} U_{ij}(Q_0, P) t_j(P) d\Gamma - \int_{\Gamma} T_{ij}(Q_0, P) u_j(P) d\Gamma, \quad (1)$$

$$\sigma_{ij}(Q_0) = \int_{\Gamma} D_{ijk}(Q_0, P) t_k(P) d\Gamma - \int_{\Gamma} S_{ijk}(Q_0, P) u_k(P) d\Gamma, \quad (2)$$

$$u_{i,k}(Q_0) = \int_{\Gamma} W_{ijk}(Q_0, P) t_j(P) d\Gamma - \int_{\Gamma} V_{ijk}(Q_0, P) u_j(P) d\Gamma, \quad (3)$$

$$C_{ij}(P_0) u_j(P_0) = \int_{\Gamma} U_{ij}(P_0, P) t_j(P) d\Gamma - \int_{\Gamma} T_{ij}(P_0, P) u_j(P) d\Gamma, \quad (4)$$

$$\frac{1}{2} \sigma_{ij}(P_0) = \int_{\Gamma} D_{ijk}(P_0, P) t_k(P) d\Gamma - \int_{\Gamma} S_{ijk}(P_0, P) u_k(P) d\Gamma, \quad (5)$$

$$C_{ikjl} u_{j,l}(P_0) = \int_{\Gamma} W_{ijk}(P_0, P) t_j(P) d\Gamma - \int_{\Gamma} V_{ijk}(P_0, P) u_j(P) d\Gamma, \quad (6)$$

where

- Q_0 and P_0 : the source points inside the domain and at the boundary, respectively ($Q_0 \in \Omega$, $P_0 \in \Gamma$);
- P : a field point located at the boundary ($P \in \Gamma$);
- $u_j(P), t_j(P), \sigma_{ij}(P)$ and $u_{i,k}(P)$: represent, respectively, the displacement, traction, stress tensor, and displacement derivative components at a point P ;
- $U_{ij}(P_0, P), T_{ij}(P_0, P), D_{ijk}(P_0, P), S_{ijk}(P_0, P), W_{ijk}(P_0, P), V_{ijk}(P_0, P)$: the fundamental solutions or the kernels;
- C_{ij} and C_{ijkl} : Free terms that depend on the nature of the boundary. For a smooth boundary they are given by

$$C_{ij} = \begin{cases} 1/2 & i = j, \\ 0 & i \neq j, \end{cases} \quad \text{and} \quad C_{ijkl} = \begin{cases} 1/2 & ik = jl, \\ 0 & ik \neq jl. \end{cases}$$

Equations (1), (2), (3) give the displacement, the stress and the displacement derivative at an internal source point $Q_0 \in \Omega$, respectively. They are expressed in terms of the boundary variables $u_j(P)$ and $t_j(P)$ at a field point $P \in \Gamma$.

Equations (4), (5) and (6) are called boundary integral equations (BIEs). For a source point located at the boundary $P_0 \in \Gamma$, they give the same quantities as (1), (2), (3), respectively. To solve (1)–(6), the boundary Γ is discretized into a finite number N of iso-parametric elements. Each element Γ_n is composed of M nodes. Equations (1)–(6) can then be written in their discrete forms as

$$\begin{aligned} u_i(Q_0) = & \sum_{n=1}^N \sum_{m=1}^M \int_{-1}^1 [U_{ij}(Q_0, P(\xi)) \psi_m(\xi) |J_n(\xi)|] d\xi \quad t_j^{nm} \\ & - \sum_{n=1}^N \sum_{m=1}^M \int_{-1}^1 [T_{ij}(Q_0, P(\xi)) \psi_m(\xi) |J_n(\xi)|] d\xi \quad u_j^{nm}, \end{aligned} \quad (7)$$

$$\begin{aligned}\sigma_{ij}(Q_0) &= \sum_{n=1}^N \sum_{m=1}^M \int_{-1}^1 [D_{ijk}(Q_0, P(\xi)) \psi_m(\xi) |J_n(\xi)|] d\xi \quad t_k^{nm} \\ &\quad - \sum_{n=1}^N \sum_{m=1}^M \int_{-1}^1 [S_{ijk}(Q_0, P(\xi)) \psi_m(\xi) |J_n(\xi)|] d\xi \quad u_k^{nm},\end{aligned}\quad (8)$$

$$\begin{aligned}u_{i,k}(Q_0) &= \sum_{n=1}^N \sum_{m=1}^M \int_{-1}^1 [W_{ijk}(Q_0, P(\xi)) \psi_m(\xi) |J_n(\xi)|] d\xi \quad t_j^{nm} \\ &\quad - \sum_{n=1}^N \sum_{m=1}^M \int_{-1}^1 [V_{ijk}(Q_0, P(\xi)) \psi_m(\xi) |J_n(\xi)|] d\xi \quad u_j^{nm},\end{aligned}\quad (9)$$

$$\begin{aligned}C_{ij}(P_0)u_j(P_0) &+ \sum_{n=1}^N \sum_{m=1}^M \int_{-1}^1 [T_{ij}(P_0, P(\xi)) \psi_m(\xi) |J_n(\xi)|] d\xi \quad u_j^{nm} \\ &= \sum_{n=1}^N \sum_{m=1}^M \int_{-1}^1 [U_{ij}(P_0, P(\xi)) \psi_m(\xi) |J_n(\xi)|] d\xi \quad t_j^{nm},\end{aligned}\quad (10)$$

$$\begin{aligned}\frac{1}{2}\sigma_{ij}(P_0) &= \sum_{n=1}^N \sum_{m=1}^M \int_{-1}^1 [D_{ijk}(P_0, P(\xi)) \psi_m(\xi) |J_n(\xi)|] d\xi \quad t_k^{nm} \\ &\quad - \sum_{n=1}^N \sum_{m=1}^M \int_{-1}^1 [S_{ijk}(P_0, P(\xi)) \psi_m(\xi) |J_n(\xi)|] d\xi \quad u_k^{nm},\end{aligned}\quad (11)$$

$$\begin{aligned}C_{ikjl}u_{j,l}(P_0) &= \sum_{n=1}^N \sum_{m=1}^M \int_{-1}^1 [W_{ijk}(P_0, P(\xi)) \psi_m(\xi) |J_n(\xi)|] d\xi \quad t_j^{nm} \\ &\quad - \sum_{n=1}^N \sum_{m=1}^M \int_{-1}^1 [V_{ijk}(P_0, P(\xi)) \psi_m(\xi) |J_n(\xi)|] d\xi \quad u_j^{nm}.\end{aligned}\quad (12)$$

From (7)–(12), we deduce that the boundary integrals involved in a BEM analysis have the general form:

$$I = \int_{-1}^1 [F(P_0, P(\xi)) \psi_m(\xi) |J_n(\xi)|] d\xi, \quad (13)$$

where

- $F(P_0, P(\xi))$: One of the fundamental solutions (kernels)
 $\{U_{ij}, T_{ij}, D_{ijk}, S_{ijk}, W_{ijk}, V_{ijk}\};$

- $\psi_m(\xi)$: The linear shape function corresponding to the node of index m ;
- $|J_n(\xi)|$: The Jacobian of the coordinate transformation from $d\Gamma$ to $d\xi$, corresponding to the element of index n .

3 The proposed integration criterion

Most of the existing integration criteria are developed under the assumption of simplified forms of integrands, such as $\left\{f(\xi) = \frac{1}{r(\xi)^p} \quad p = 1, 2, 3\right\}$ and $\left\{f(\xi) = \log\left(\frac{1}{r(\xi)}\right)\right\}$. Some criteria also incorporate shape functions and the Jacobian with $\left\{f(\xi) = \frac{1}{r(\xi)^p} \cdot \psi_m(\xi) \cdot J_n(\xi) \quad p = 1, 2\right\}$, as done by Eberwien, Duencer, and Moser [10]. These simplified assumptions yield satisfactory results in structures that are not extremely thin, especially in scalar problems like electrostatics, where kernel functions are typically simple. However, elasticity problems are vectorial in nature, involving heavy kernel functions that include directional and normal derivatives of the distance r . These complexities can exacerbate singularities and amplify the boundary layer effect in extremely thin structures. As a result, we are motivated to investigate the actual distribution of integration errors by considering the complete form of integrands encountered in planar elastic boundary element analysis and comparing them with simplified integrands. Subsequently, we propose a numerical scheme with a new criterion aimed at meeting high precision requirements, even in extremely thin structures, while optimizing computational resources and CPU time.

3.1 The numerical testing

Due to the absence of mathematical tools and techniques to define analytically error bounds for integrands in their complete form as specified in (13), numerical experimentation remains the primary recourse. The numerical testing methodology followed by Eberwien, Duencer, and Moser [10] is

adopted. It involves the utilization of a rectangular region encompassing a reference quadratic iso-parametric element. Within this region, a highly dense grid of points is established, creating the illusion of a continuous area. Two iso-parametric elements are considered, one flat and the other slightly curved (Figure 3). The relative error under consideration is determined as the maximum value obtained from these two reference elements.



Figure 3: The two reference boundary elements

The numerical experimentation strategy involves evaluating the boundary integrals at each point of the dense grid twice. Initially, the first integral, I_N , is computed using a prescribed Gauss order N . Subsequently, a reference integral, I_{100} , is calculated with a fixed 100 Gauss points. Next, for each point P , the relative error is determined as $\epsilon(P) \approx \left| \frac{I_N(P) - I_{100}(P)}{I_{100}(P)} \right|$. Once the distribution of the relative errors is established, an iso-error curve, or an error contour curve (as named in [4]), is plotted for a target maximum relative error, ϵ_0 . From this curve, the minimum allowable ratio $\lambda_0 = \frac{r_0}{L}$ is derived, ensuring a relative error $\epsilon < \epsilon_0$ for $\lambda = \frac{r}{L} > \lambda_0$.

By repeating the steps described above for various Gauss orders, a curve $N = f(\lambda)$ is constructed. By utilizing curve fitting techniques, an empirical formula is derived to express the number of Gauss points N as a function of the λ ratio. This process is conducted for various orders of singularity, including $\{\log(\frac{1}{r}), \frac{1}{r}, \frac{1}{r^2}\}$, and for three target maximal relative errors $\epsilon_0 = 10^{-2}, 10^{-3}, 10^{-4}$.

Numerical tests are conducted on two cases. The first case represents the lower limit, where errors are underestimated by assuming simplified integrands that only include terms responsible for the singularity. In contrast, the second case provides a realistic estimation of the error by considering the complete expressions of the kernels, shape functions, and the Jacobian, as outlined in (13).

3.1.1 Case one: Simplified integrands

The following integrals are considered:

$$\begin{cases} I_1 = \int_{-1}^1 \log\left(\frac{1}{r(\xi)}\right) d\xi & \Rightarrow O\left(\log\left(\frac{1}{r}\right)\right), \\ I_2 = \int_{-1}^1 \frac{1}{r(\xi)} d\xi & \Rightarrow O\left(\frac{1}{r}\right), \\ I_3 = \int_{-1}^1 \frac{1}{r(\xi)^2} d\xi & \Rightarrow O\left(\frac{1}{r^2}\right). \end{cases}$$

For each integral, the procedure detailed in section 3.1 is executed.

The resulting iso-error curves exhibit a closed form characterized by multiple lobes, akin to those observed in the work [10]. These distinctive curves, commonly referred to as butterfly curves, are depicted in Figures 4 and 5. The dataset in Table 1 defines, for the lower limit case, the minimum allowable ratios λ_0 for quadrature orders ranging from 2 to 35. These results are computed for singularity orders of $\{\log(\frac{1}{r}), \frac{1}{r}, \frac{1}{r^2}\}$, and precisions $\epsilon_0 = 10^{-2}, 10^{-3}, 10^{-4}$.

Table 1 shows that the minimum allowable ratio λ_0 decreases with increasing Gauss order N , as fewer Gauss points lead to higher errors, requiring greater distances from the boundary to stay below the error threshold. This effect intensifies with stronger singularities, especially for $O(\frac{1}{r^2})$, and as the error threshold ϵ_0 becomes stricter, with the highest λ_0 observed at $\epsilon_0 = 10^{-4}$.

3.1.2 Case two: Full form integrands

In this case the full form of integrals given in (13) is considered:

$$I = \int_{-1}^1 F(P_0, P(\xi)) \cdot \psi_m(\xi) \cdot J(\xi) d\xi,$$

where $F(P_0, P(\xi))$ is one of the fundamental solutions (kernels) $\{U_{ij}, T_{ij}, D_{ijk}, S_{ijk}, W_{ijk}, V_{ijk}\}$

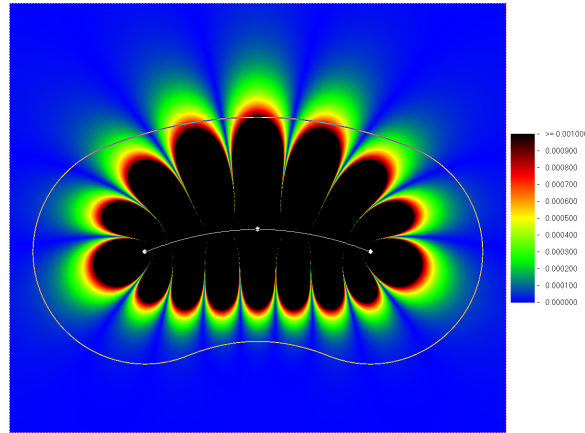


Figure 4: Relative error distribution around the curved reference element, for integral I_2 with 4 Gauss points

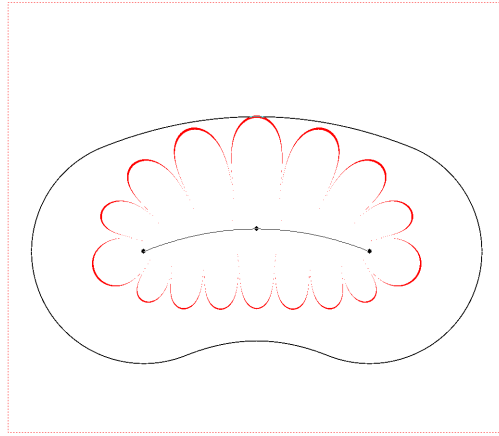


Figure 5: Iso-error curve and envelope, corresponding to integral I_2 with 4 Gauss points and a relative error 10^{-3}

$$\begin{cases} F(P_0, P(\xi)) = U_{ij} & \Rightarrow O\left(\log\left(\frac{1}{r}\right)\right), \\ F(P_0, P(\xi)) = T_{ij}, D_{ijk}, W_{ijk} & \Rightarrow O\left(\frac{1}{r}\right), \\ F(P_0, P(\xi)) = S_{ijk}, V_{ijk} & \Rightarrow O\left(\frac{1}{r^2}\right). \end{cases}$$

The relative error is computed for each function by varying the indices $i = 1, 2; j = 1, 2; k = 1, 2; m = 1, 2, 3$ to encompass all possible combinations, from which the maximum error is identified. Subsequently, the maximum

Table 1: The numerical results obtained for the lower limit case

Precision	$\epsilon_0 = 10^{-2}$			$\epsilon_0 = 10^{-3}$			$\epsilon_0 = 10^{-4}$		
	$O(\log(\frac{1}{r}))$	$O(\frac{1}{r})$	$O(\frac{1}{r^2})$	$O(\log(\frac{1}{r}))$	$O(\frac{1}{r})$	$O(\frac{1}{r^2})$	$O(\log(\frac{1}{r}))$	$O(\frac{1}{r})$	$O(\frac{1}{r^2})$
2	1.125718	0.732523	1.053462	1.722896	1.69977	2.476304	3.119036	4.06014	6.231677
3	0.378903	0.39962	0.554979	1.047436	0.749395	1.00197	1.396343	1.318512	1.759226
4	0.223531	0.274538	0.378153	0.472037	0.483714	0.628713	1.010303	0.76963	0.981932
5	0.154594	0.21098	0.290135	0.310726	0.357336	0.460149	0.535374	0.540789	0.676164
6	0.11511	0.169262	0.235735	0.234901	0.28358	0.364319	0.381201	0.419096	0.517973
7	0.093778	0.142997	0.19878	0.188934	0.235656	0.301954	0.300095	0.342807	0.422116
8	0.076123	0.122481	0.171704	0.156941	0.201674	0.258723	0.248345	0.290531	0.356786
9	0.065062	0.107721	0.151201	0.133973	0.175814	0.225891	0.211074	0.251334	0.307793
10	0.055238	0.09541	0.134793	0.115931	0.156121	0.200444	0.183201	0.221721	0.272248
11	0.048691	0.086535	0.121919	0.103183	0.140165	0.180581	0.161941	0.198604	0.24436
12	0.042454	0.077927	0.111508	0.091398	0.126997	0.164631	0.145019	0.179886	0.220847
13	0.038029	0.071969	0.102493	0.083067	0.116594	0.15077	0.131184	0.164631	0.201681
14	0.033912	0.065875	0.094861	0.074748	0.107349	0.138989	0.119406	0.15146	0.186122
15	0.03105	0.061564	0.088616	0.068554	0.099716	0.129108	0.11012	0.140369	0.172947
16	0.027884	0.057352	0.082592	0.063127	0.092762	0.12079	0.101328	0.130294	0.161163
17	0.025693	0.054003	0.077653	0.058508	0.086813	0.11317	0.09407	0.122375	0.150767
18	0.023196	0.050654	0.07316	0.05407	0.081657	0.10693	0.087638	0.114613	0.141575
19	0.021674	0.047976	0.069224	0.050654	0.077048	0.100757	0.082193	0.107954	0.133874
20	0.019848	0.045297	0.065766	0.047306	0.073029	0.095438	0.076952	0.101978	0.126629
21	0.018508	0.043105	0.062709	0.044644	0.069224	0.090771	0.07297	0.096695	0.120459
22	0.017054	0.040698	0.05969	0.042248	0.065891	0.08681	0.068605	0.092073	0.114522
23	0.015891	0.039147	0.056977	0.039922	0.062791	0.082871	0.065434	0.08811	0.109204
24	0.015116	0.037209	0.054651	0.037597	0.060078	0.079265	0.061669	0.08415	0.104181
25	0.013953	0.035659	0.052713	0.036047	0.057364	0.076128	0.059154	0.080194	0.099794
26	0.013178	0.034109	0.050388	0.034109	0.055201	0.072991	0.05637	0.076993	0.096029
27	0.012403	0.032946	0.048837	0.032558	0.053101	0.070205	0.053876	0.074054	0.092266
28	0.011598	0.031701	0.046796	0.030928	0.051179	0.067698	0.051619	0.071368	0.089129
29	0.011082	0.03067	0.045249	0.029639	0.049374	0.065206	0.049548	0.068712	0.085678
30	0.010567	0.029381	0.043702	0.028351	0.047569	0.062952	0.047484	0.066279	0.082934
31	0.010052	0.028608	0.042413	0.02732	0.046022	0.060976	0.045935	0.064	0.080128
32	0.009278	0.027577	0.041123	0.026031	0.044475	0.059171	0.044072	0.061952	0.077605
33	0.009021	0.026546	0.039834	0.025258	0.043186	0.057366	0.042526	0.060129	0.075173
34	0.008505	0.025773	0.038545	0.024227	0.041639	0.055562	0.040979	0.058065	0.072906
35	0.008247	0.025	0.037514	0.023196	0.040608	0.054015	0.039691	0.056516	0.070641

error value is selected among functions sharing the same singularity order, as follows:

$$\begin{cases} \epsilon_{\max}\left(O\left(\log\left(\frac{1}{r}\right)\right)\right) &= \epsilon_{\max}(U_{ij}), \\ \epsilon_{\max}\left(O\left(\frac{1}{r}\right)\right) &= \max(\epsilon_{\max}(T_{ij}), \epsilon_{\max}(D_{ijk}), \epsilon_{\max}(W_{ijk})), \\ \epsilon_{\max}\left(O\left(\frac{1}{r^2}\right)\right) &= \max(\epsilon_{\max}(S_{ijk}), \epsilon_{\max}(V_{ijk})), \end{cases}$$

In this case, the iso-error curves obtained do not exhibit closed contours akin to those described in section 3.1.1. Rather, they feature sharp filaments that become thinner as they extend further from the element (Figures 6–7). This characteristic is particularly noticeable when lower Gaussian or-

ders are employed. Generating envelopes for the iso-error curves is not as straightforward as in the previous case. Therefore, the adopted solution is to solely consider the points located within denser regions of the iso-error curve. Specifically, a point is considered valid only if it has at least three adjacent points that have an error greater than or equal to the target error. This automated approach yields satisfactory results, as depicted in Figures 6 and 7. Another notable observation is that numerical testing with fewer than 4 Gauss points results in significantly large errors and exceedingly high λ_0 ratios. Consequently, quadrature orders of 2 and 3 cannot be considered in this case.

The dataset in Table 2 defines, for the upper limit case, the minimum allowable ratios λ_0 for quadrature orders ranging from 4 to 35. These results are computed for singularity orders of $\{\log(\frac{1}{r}), \frac{1}{r}, \frac{1}{r^2}\}$, and precisions $\epsilon_0 = 10^{-2}, 10^{-3}, 10^{-4}$.

The same patterns observed in Table 1 regarding the variation of λ_0 with respect to Gauss order N , singularity order, and the imposed error threshold are also evident in Table 2. Notably, the λ_0 values in Table 2 are significantly higher than their counterparts in Table 1, which can be attributed to the consideration of the full form of the integrals.

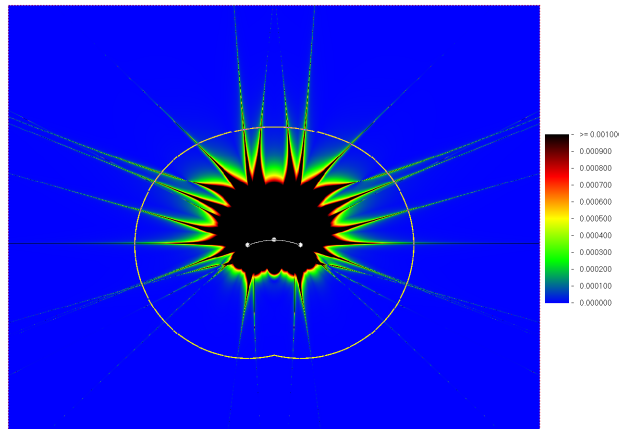
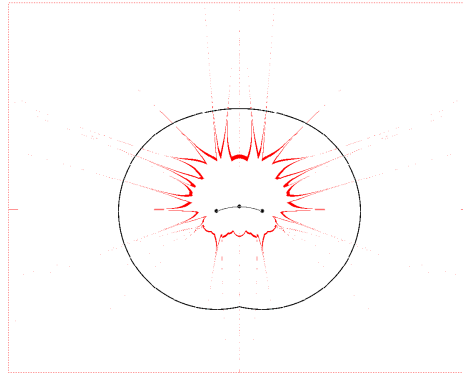


Figure 6: Relative error distribution around the reference curved element, for integral with T_{ij} kernel with 5 Gauss points

Table 2: The numerical results obtained for the upper limit case

Precision	$\epsilon_0 = 10^{-2}$			$\epsilon_0 = 10^{-3}$			$\epsilon_0 = 10^{-4}$		
	$O(\log(\frac{1}{\epsilon}))$	$O(\frac{1}{\epsilon})$	$O(\frac{1}{\epsilon^2})$	$O(\log(\frac{1}{\epsilon}))$	$O(\frac{1}{\epsilon})$	$O(\frac{1}{\epsilon^2})$	$O(\log(\frac{1}{\epsilon}))$	$O(\frac{1}{\epsilon})$	$O(\frac{1}{\epsilon^2})$
4	1.731452	3.466213	4.605432	2.26537	5.621703	9.956321			
5	0.990553	1.789411	2.234695	1.549063	2.258132	2.916322	1.916653	4.349683	5.034239
6	0.641329	1.210843	1.446829	0.847523	1.485321	1.71883	1.291281	2.211769	2.869445
7	0.506101	0.869918	0.948868	0.644162	1.147801	1.28719	0.938622	1.470089	1.717305
8	0.40158	0.594745	0.703197	0.483972	0.798056	0.936451	0.659695	1.09948	1.179583
9	0.339498	0.509217	0.621206	0.418563	0.610964	0.764019	0.567532	0.786614	0.98676
10	0.287768	0.441216	0.576349	0.346524	0.529581	0.670176	0.463009	0.662586	0.795725
11	0.24508	0.392913	0.524175	0.307237	0.458307	0.577628	0.411636	0.551755	0.6866
12	0.217618	0.361741	0.44923	0.265209	0.419566	0.533782	0.363731	0.494877	0.613864
13	0.184143	0.329125	0.404135	0.232998	0.384247	0.462339	0.316576	0.437666	0.561505
14	0.172671	0.302964	0.371398	0.219531	0.360468	0.438523	0.288139	0.40124	0.527596
15	0.153868	0.296416	0.349031	0.201693	0.337231	0.401847	0.255058	0.36921	0.451162
16	0.14172	0.258965	0.319079	0.183379	0.308434	0.361102	0.228336	0.342827	0.40318
17	0.13214	0.22594	0.309555	0.168858	0.295729	0.343361	0.211628	0.31895	0.365151
18	0.127365	0.209414	0.276741	0.163691	0.261573	0.323737	0.198633	0.307648	0.346978
19	0.119226	0.197478	0.261351	0.15	0.244915	0.315091	0.187495	0.300695	0.334115
20	0.111972	0.188242	0.232066	0.142254	0.230969	0.30471	0.178216	0.272005	0.323738
21	0.108583	0.178362	0.211824	0.136444	0.216996	0.273097	0.168004	0.243959	0.315953
22	0.102817	0.169428	0.202378	0.130282	0.199078	0.262495	0.160862	0.237681	0.31163
23	0.098592	0.166204	0.198193	0.125306	0.189353	0.226737	0.155008	0.225242	0.271844
24	0.09507	0.165334	0.186731	0.119718	0.185464	0.216276	0.147583	0.222462	0.245897
25	0.091549	0.164062	0.175876	0.115096	0.170425	0.208829	0.142943	0.20568	0.233789
26	0.088028	0.163364	0.172232	0.111383	0.162875	0.191682	0.136445	0.185374	0.221683
27	0.085211	0.145735	0.165063	0.107042	0.158314	0.186731	0.130875	0.184582	0.213032
28	0.082394	0.136129	0.158037	0.103957	0.154121	0.181879	0.128091	0.172242	0.202653
29	0.079577	0.134008	0.155645	0.100245	0.14795	0.177025	0.123084	0.167684	0.194871
30	0.077465	0.132594	0.151986	0.097183	0.144613	0.167816	0.117881	0.163207	0.188816
31	0.075184	0.130938	0.144066	0.093747	0.14207	0.166256	0.115096	0.158548	0.180169
32	0.072535	0.129645	0.14263	0.091549	0.138743	0.16298	0.111384	0.154713	0.174119
33	0.070423	0.128353	0.134518	0.089106	0.136108	0.161409	0.107671	0.15079	0.16897
34	0.069014	0.127706	0.131838	0.086322	0.134169	0.151348	0.103958	0.146912	0.164346
35	0.066901	0.124931	0.128298	0.083803	0.13223	0.149121	0.101984	0.145145	0.159715

Figure 7: Iso-error curve and envelope, corresponding to integral with T_{ij} kernel with 5 Gauss points and a target relative error 10^{-3}

3.2 Determination of the empirical formulas for the two limit cases

Tables 1 and 2 present the numerically obtained results for the lower and upper limit cases, respectively. These data are then translated into two empirical formulas aimed at determining the Gauss order N necessary to attain a desired precision (10^{-2} , 10^{-3} and 10^{-4}) for a given λ ratio. The empirical formulas are deduced using curve-fitting techniques, assuming an exponential decay profile that closely mirrors the relationship between N and the λ ratio.

3.2.1 The lower limit curve

Based on the numerical results in Table 1, Figure 8 presents the variation curves of the required Gauss order N versus the minimum allowable ratio λ_0 for three singularity orders: $O\left(\log\left(\frac{1}{r}\right)\right)$, $O\left(\frac{1}{r}\right)$ and $O\left(\frac{1}{r^2}\right)$, with a target error of $\epsilon_0 = 10^{-3}$.

A closer examination of the three graphs shown in Figure 8 reveals a clear exponential decay pattern in the relationship between the Gauss order N and the ratio λ_0 . Specifically, the curves decrease from infinity and approach a horizontal asymptote at $N = 2$. This behavior is consistently observed for the other error thresholds as well, namely $\epsilon_0 = 10^{-2}$ and $\epsilon_0 = 10^{-4}$.

Consequently, we propose the following formula:

$$N_l(\lambda) = 2 + A_l \times \lambda^{B_l}, \quad (14)$$

where A_l and B_l are constants, with $A_l > 0$, $B_l < 0$ and $\lambda = \frac{r}{L}$.

N.B. The subscript “l” stands for **L**ower limit curve.

$$\begin{cases} \lim_{\lambda \rightarrow 0} N_l(\lambda) = +\infty, \\ \lim_{\lambda \rightarrow +\infty} N_l(\lambda) = 2. \end{cases} \quad (15)$$

The coefficients A_l and B_l are derived through exponential curve fitting. The

results are outlined in Table 3. Figure 9 displays the variation curves of the required Gauss order N needed to achieve a target precision of $\epsilon_0 = 10^{-3}$ for a singularity of order $O\left(\frac{1}{r}\right)$, based on both the empirical formula in (14) and the numerical results from Table 1.

A closer examination of the two graphs in Figure 9 reveals strong agreement between the numerical data and its empirical representation by 14. This consistency also holds for the other singularity orders $\{O\left(\log\left(\frac{1}{r}\right)\right), O\left(\frac{1}{r^2}\right)\}$ and error thresholds $\{10^{-2}, 10^{-4}\}$.

Table 3: A_l and B_l coefficients for the lower limit curve

	$\epsilon_0 = 10^{-2}$		$\epsilon_0 = 10^{-3}$		$\epsilon_0 = 10^{-4}$	
	A_l	B_l	A_l	B_l	A_l	B_l
$O\left(\log\left(\frac{1}{r}\right)\right)$	0.9923	-0.7332	1.226	-0.8785	1.693	-0.9214
$O\left(\frac{1}{r}\right)$	0.6712	-1.059	1.133	-1.054	1.695	-1.034
$O\left(\frac{1}{r^2}\right)$	0.8708	-1.11	1.419	-1.08	2.052	-1.049

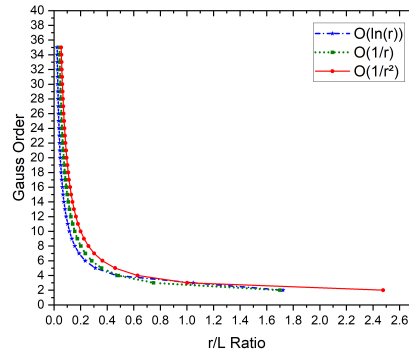


Figure 8: Numerical results of variation of N as function of λ ratio for lower limit case with a precision 10^{-3}

3.2.2 The upper limit curve

Similar to Figure 8, Figure 10 illustrates the variation of N with respect to the minimum allowable ratio λ_0 , based on the numerical results of the full-form

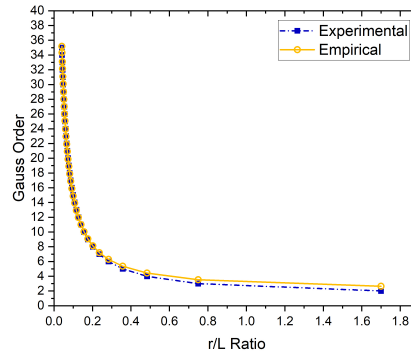


Figure 9: Comparison between empirical formula of (14) and numerical results of the lower limit case with singularity $O\left(\frac{1}{r}\right)$ and precision 10^{-3}

integrands, as recorded in Table 2, for a target error bound of $\epsilon_0 = 10^{-3}$.

An analysis of the curves in Figure 10 reveals a similar exponential decay pattern; however, in this case, the horizontal asymptote is located at $N = 4$ instead of $N = 2$.

Accordingly, we propose another empirical formula analogous to that previously introduced in (14).

$$N_u(\lambda) = 4 + A_u \times \lambda^{B_u}, \quad (16)$$

where A_u and B_u are constants, with $A_u > 0, B_u < 0$ and $\lambda = \frac{r}{L}$.

N.B. The subscript “u” stands for Upper limit curve.

$$\begin{cases} \lim_{\lambda \rightarrow 0} N_u(\lambda) = +\infty, \\ \lim_{\lambda \rightarrow +\infty} N_u(\lambda) = 4. \end{cases} \quad (17)$$

Similar to section 3.2.1, the coefficients A_u and B_u are derived through exponential curve fitting techniques. The results are outlined in Table 4 To validate the consistency of the empirical formula in (16) with the numerical results in Table 2, Figure 11 illustrates the variation of the Gauss order N as a function of λ , required to achieve a target accuracy of $\epsilon_0 = 10^{-3}$ for a singularity of order $O\left(\frac{1}{r}\right)$. The figure compares the predictions of the empirical

model with the corresponding numerical data.

A detailed comparison of the two curves in Figure 11 reveals excellent agreement between the empirical and numerical results. This consistency also extends to rest cases involving different singularity orders $\{O(\log(\frac{1}{r})), O(\frac{1}{r^2})\}$ and alternative error thresholds, including $\{10^{-2}, 10^{-4}\}$.

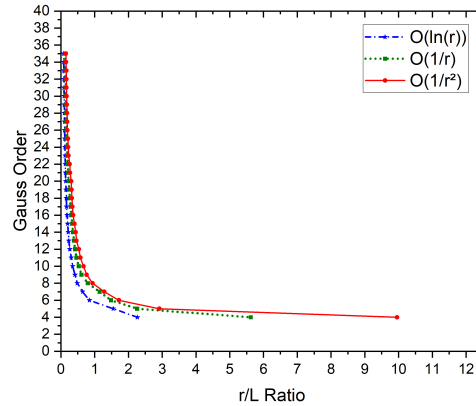


Figure 10: Experimental upper limit curves of variation of N as function of λ ratio in case of precision 10^{-3}

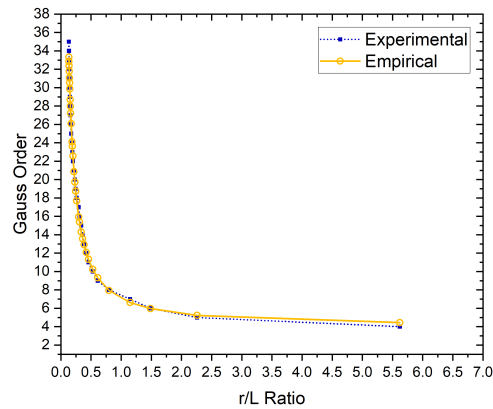


Figure 11: Comparison between empirical formula and experimental results for the case of the upper limit curve $O(\frac{1}{r})$ and precision 10^{-3}

Table 4: A_u and B_u coefficients for the upper limit curve

	$\epsilon_0 = 10^{-2}$		$\epsilon_0 = 10^{-3}$		$\epsilon_0 = 10^{-4}$	
	A_u	B_u	A_u	B_u	A_u	B_u
$O\left(\log\left(\frac{1}{r}\right)\right)$	1.169	-1.21	1.596	-1.195	2.376	-1.12
$O\left(\frac{1}{r}\right)$	2.002	-1.283	3.065	-1.116	3.953	-1.048
$O\left(\frac{1}{r^2}\right)$	3.323	-1.082	4.2	-1.038	5.16	-0.9721

3.3 Determination of the generalized empirical formula of the proposed integration criterion

While the lower limit formula of (14) offers improved performance by reducing computational time, it tends to yield less accurate results. Conversely, the upper limit formula of (16) achieves high accuracy but at the expense of significantly slower performance. Therefore, an optimal approach requires striking a balance between performance and accuracy. This is accomplished by introducing a formula that describes a curve positioned between the two defined extremes, leaning toward one limit or the other depending on the structure type or the method employed for near-singular treatment. This approach can be particularly useful in the case of variable transformation techniques and semi-analytical algorithms that reduce or cancel the boundary layer effect, where unnecessary computational overhead can be avoided to take full advantage of these techniques.

For instance, in the case of a thin structure analyzed solely through the element subdivision method with a straightforward application of the Gaussian integration technique, a curve closer to the upper limit is preferable. However, when employing a nonlinear transformation technique to address the same problem, the curve can be shifted toward the lower limit, thereby conserving computational resources. A parameter $\alpha \in [0, 1]$ is introduced to control the curve position, such that $\alpha = 0$ corresponds to the lower curve and $\alpha = 1$ to the upper curve. Any value of α between 0 and 1 produces an intermediate curve.

Equations (14) and (16), are written in the new following form:

$$\begin{cases} N_l(\lambda) = N_{0_l} + A_l \times \lambda^{B_l}, \\ N_u(\lambda) = N_{0_u} + A_u \times \lambda^{B_u}, \end{cases} \quad (18)$$

where $N_{0_l} = 2, N_{0_u} = 4, (A_l, B_l)$ are given in Table 3 and (A_u, B_u) is given in Table 4.

To maintain the same exponential profile observed in the lower and upper limit curves, we propose a formula similar to (14) and (16).

$$N(\lambda, \alpha) = N_0(\alpha) + A(\alpha) \times \lambda^{B(\alpha)}, \quad (19)$$

where $N_0(\alpha), A(\alpha)$ and $B(\alpha)$ are given as functions of the parameter α deduced by linear combinations of $(N_{0_l}, N_{0_u}), (A_l, A_u)$ and (B_l, B_u) , respectively.

Let $\{\Delta N_0 = N_{0_u} - N_{0_l} = 2\}, \{\Delta A = A_u - A_l\}$ and $\{\Delta B = B_u - B_l\}$.

The linear combinations will have the following form:

$$\begin{cases} N_0(\alpha) = N_{0_l} + \alpha \times \Delta N_0 = 2.(\alpha + 1), \\ A(\alpha) = A_l + \alpha \times \Delta A, \\ B(\alpha) = B_l + \alpha \times \Delta B. \end{cases} \quad (20)$$

Thus, (19) becomes

$$N(\lambda, \alpha) = 2.(\alpha + 1) + A(\alpha) \times \lambda^{B(\alpha)} \quad (21)$$

with the functions $A(\alpha)$ and $B(\alpha)$ given in Table 5.

Table 5: $A(\alpha)$ and $B(\alpha)$ functions for our final empirical formula

	$\epsilon_0 = 10^{-2}$		$\epsilon_0 = 10^{-3}$		$\epsilon_0 = 10^{-4}$	
	$A(\alpha)$	$B(\alpha)$	$A(\alpha)$	$B(\alpha)$	$A(\alpha)$	$B(\alpha)$
$O(\log(\frac{1}{\epsilon}))$	$0.9923 + 0.1767\alpha$	$-0.7332 - 0.4768\alpha$	$1.226 + 0.37\alpha$	$-0.8785 - 0.3165\alpha$	$1.693 + 0.683\alpha$	$-0.9214 - 0.1986\alpha$
$O(\frac{1}{\epsilon})$	$0.6712 + 1.3308\alpha$	$-1.059 - 0.224\alpha$	$1.133 + 1.932\alpha$	$-1.054 - 0.062\alpha$	$1.695 + 2.258\alpha$	$-1.034 - 0.014\alpha$
$O(\frac{1}{\epsilon^2})$	$0.8708 + 2.4522\alpha$	$-1.11 + 0.028\alpha$	$1.419 + 2.781\alpha$	$-1.08 + 0.042\alpha$	$2.052 + 3.108\alpha$	$-1.049 + 0.0769\alpha$

We propose a new integration criterion for the 2D elasticity BEM, defined by the empirical formula in (21). The corresponding linear functions $A(\alpha)$ and $B(\alpha)$ are listed in Table 5. The parameter α is application-dependent

and may vary according to factors such as the thinness of the structure or the use of near-singular treatment techniques. Figure 12 presents a series of curves generated with the proposed empirical formula for a singularity of order $O(\frac{1}{r})$, with a target accuracy of 10^{-3} . These curves lie consistently between the two limiting curves and display a uniform exponential behavior. The proposed empirical formula of (21), like existing ones, follows an exponential form that naturally leads to very high Gauss quadrature orders for small λ ratios. This behavior is consistent with the formulations in (15) and (17). However, excessively high quadrature orders may introduce floating-point round-off errors. Moreover, computing or retrieving the corresponding Gauss–Legendre nodes and weights at runtime can create significant performance bottlenecks.

To overcome this issue, most BEM software relies on precomputed tables of Gauss–Legendre nodes and weights. Consequently, when (21) prescribes a Gauss order exceeding the available predefined values, the element must be subdivided. To address this, we provide an additional formula to determine the required number of subelements:

$$M = \frac{1}{\lambda} \times \left(\frac{N_{avl} - 2(1 + \alpha)}{A(\alpha)} \right)^{\frac{1}{B(\alpha)}} + 1, \quad (22)$$

where M is the number of subelements and N_{avl} is the maximum Gauss order available in the program.

3.4 Guidelines on the choice of the α parameter

An optimal selection of the parameter α would require a comprehensive optimization study that considers multiple factors, including the geometry of the structure, the value of the ratio λ , and the type of variable transformation technique if any is employed. Such an in-depth investigation is not addressed in the current manuscript.

Nevertheless, preliminary guidance for choosing α can be provided based on practical experience and supported by the results from the validation example presented in Section 4. Table 6 summarizes these guidelines with respect to

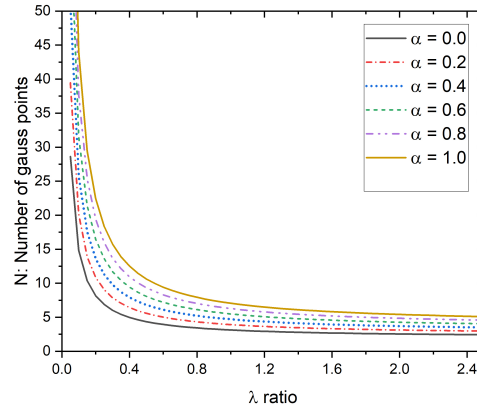


Figure 12: Limit and intermediate curves of the new criterion, singularity order $O(\frac{1}{r})$ and precision 10^{-3}

structural thinness and the presence or absence of near-singularity treatment techniques.

Table 6: Guidelines on the choice of the α parameter

	Nonthin structures	Moderately thin structures	Extremely thin structures
Without semi-analytical treatment	$\alpha = 0$ to 0.3	$\alpha = 0.3$ to 0.7	$\alpha = 0.7$ to 1
With semi-analytical treatment	N.A	$\alpha = 0$ to 0.3	$\alpha = 0.3$ to 0.6

3.5 Numerical implementation

One of the main advantages of the empirical formula approach is its simplicity and ease of numerical implementation. The proposed expressions can be directly coded as a function that receives the relevant input arguments and returns the required Gauss order. This function is then invoked within the subroutine that performs the numerical integration. If needed, the subroutine can subdivide the boundary element into smaller subelements and re-evaluate the corresponding Gauss order for each by calling the same func-

tion.

The implementation details of the algorithm used to perform the BEM numerical integrations, corresponding to the general form of (13), are summarized as follows: **Step 0:** To evaluate the integral I over the boundary element E with

$$I = \int_{-1}^1 f(\xi) d\xi$$

such that

$$f(\xi) = F(P^*, P(\xi)) \psi(\xi) J(\xi).$$

Gather all the necessary input data: {Source point P^* , boundary element E (of length L), the singularity order of the integration kernel $F(P^*, P(\xi))$, the selected value of α , the required precision (10^{-2} , 10^{-3} or 10^{-4}) }.

Step 1: Evaluate r : the shortest distance between the source point P^* and the boundary element E .

Step 2: Calculate the λ ratio with $\lambda = \frac{r}{L}$.

Step 3: Calculate N : the number of Gauss points necessary to obtain the target precision by using (21), which returns a real number that is rounded to the nearest integer.

Step 4: Verify if the obtained Gauss order N is less than or equal N_{avl} , the maximum available order in the program ($N \leq N_{avl}$).

Step 5: IF TRUE, evaluate the integral using N Gauss points, with

$$I = \int_{-1}^1 f(\xi) d\xi \approx \sum_{i=1}^N f(\xi_i) w_i. \quad (23)$$

Return I and terminate the algorithm.

Step 6: ELSE, the element E has to be subdivided into M subelements, with M determined through (22).

Step 7: For each subelement E_k , $\{k = 1, 2, \dots, M\}$ calculate the necessary number of Gauss points by repeating the steps from **Step 0** to **Step 3**, then calculate the integral I_k by using the following formula [1]:

$$I_k = \int_{-1}^1 f(\eta) d\eta \approx \sum_{i=1}^N f(\bar{\eta}_i) w_i \quad (24)$$

with $\bar{\eta}_i = \frac{1}{M}(M - 2k + 1 + \eta_i)$.

Step 8: Calculate the global integral over the boundary element E with

$$I \approx \frac{1}{M} \sum_{k=1}^M I_k. \quad (25)$$

Return I and terminate the algorithm.

3.6 Comparison between the proposed criterion and the existing ones

In order to compare the existing criteria with the proposed one, the corresponding functions $N(\lambda)$ are plotted on a log-log graph (Figure 13). A closer examination of the curves in Figure 13 reveals the following observations:

The formula of Lachat and Watson suggests relatively low Gauss orders for large values of the λ ratio. However, the required order increases drastically for small λ values, tending to infinity as λ approaches $\frac{1}{4}$. This behavior is confirmed by the approximation formula proposed by Gao and Davies [11], which appears in (26)–(27)

$$N(\lambda, \epsilon_0) = \frac{p' \log\left(\frac{\epsilon_0}{2}\right)}{2 \log\left(\frac{1}{4\lambda}\right)}, \quad (26)$$

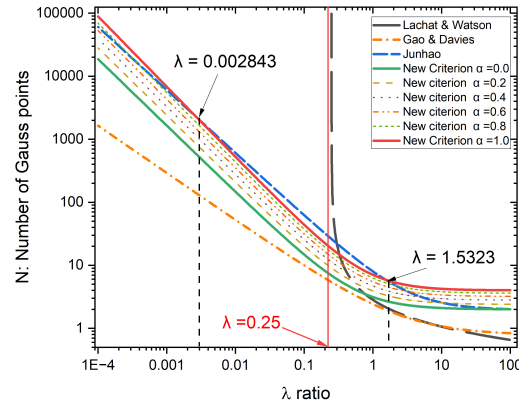
$$\lim_{\lambda \rightarrow \frac{1}{4}} N(\lambda, \epsilon_0) = \lim_{\lambda \rightarrow \frac{1}{4}} \frac{p' \log\left(\frac{\epsilon_0}{2}\right)}{2 \log\left(\frac{1}{4\lambda}\right)} = +\infty. \quad (27)$$

This divergence of the Gauss order at $\lambda \approx \frac{1}{4}$ makes the Lachat and Watson criterion very resource-consuming, introducing unnecessary computational overhead, especially in the case of thin structures. A closer look at the other curves shows that the Gao and Davies formula suggests the lowest N , making it less resource-consuming but at the expense of reduced accuracy, which will be demonstrated further in the validation example of Section 4. The newly proposed criterion, with its different values of the parameter α , appears in the log-log graph as a band of nearly parallel lines, particularly for $\lambda < 0.5$. The upper-limit curve ($\alpha = 1$) intersects with the Junhao curve at $\lambda = 0.002843$ and $\lambda = 1.5323$. Within the interval $\lambda \in [0.002843, 1.5323]$, the proposed criterion with $\alpha = 1$ suggests fewer Gauss points than the formula of [23]. For values of $\alpha < 1$, this interval becomes wider. From these observations, we note that the proposed formula produces fewer Gauss points at moderate λ values, which are predominant when element subdivision is applied, as in most BEM applications where only a limited number of Gaussian weights and abscissas are available in the program. Furthermore, it is worth noting that the numerical implementation of empirical criteria is simpler compared to

tabular criteria. In the tabular case, the programmer must check the value of the λ ratio and extract the corresponding Gauss order based on the interval in which it falls. In contrast, with the empirical approach, one only needs to pass the value of λ as an argument to the formula's function, which directly returns the appropriate Gauss order as an integer. Finally, Table 7 presents a comparative summary that situates the proposed criterion within the broader framework of existing methods while emphasizing their key distinctions.

Table 7: Recapitulative table for the comparison between the different criteria

Criterion	Form	Mathematical error estimation	Numerical testing	Intended for	Further improvements	Disadvantages
Lachat and Watson [25]	Empirical formulas	YES: Based on Stroud and Secrest [39] for $(\frac{1}{r^2})$	NO	3D structures, but usable in 2D	- Simplified by Mustoe [29] - Simplified by Gao and Davies [11]	- Less accurate in thin structures; - Diverges at $\lambda = \frac{1}{4}$, gives very high Gauss orders for small λ .
Jun and Beer [22]	Table format	YES: Based on Stroud and Secrest [39] for $(\frac{1}{r}, \frac{1}{r^2}, \frac{1}{r^3})$	NO	Both 3D and 2D		- Less accurate in thin structures; - Table format only.
Bu and Davies [4]	Empirical + Table	NO	YES: Testing on $(\frac{1}{r}, \frac{1}{r^2}, \frac{1}{r^3})$	3D structures, usable in 2D	Simplified by Gao and Davies [11]	Less accurate in thin structures.
Eberwien, Duencer, and Moser [10]	Table format	NO	YES: Testing on $f(\xi) = \frac{1}{r^p} \Psi(\xi) J(\xi)$, $p \in \{1, 2\}$	2D structures		Table format only.
Junhao, Zhipeng, and Yongqiang [23]	Empirical formulas	NO	YES: Testing on $(\ln(\frac{1}{r}), \frac{1}{r}, \frac{1}{r^2})$	2D structures		Computational gain only for very small λ (rare in element subdivision).
Zhou, Yang, and Chen [48]	Neural network (AI)	NO	YES: NN trained to propose Gauss order (depends on source point, geometry, kernel, ...)	2D structures		Needs a trained neural network.
Proposed criterion	Empirical formulas	NO	YES: Testing on full kernel functions of 2D elasticity BEM	Tailored for 2D elasticity (extendable to other 2D apps)		Requires choice of control parameter α .

Figure 13: Variation of N versus λ for the new criterion and existing ones

4 Validation example

Let us consider a long and very thin fin, characterized by a length $L = 10$ cm and a maximum height $H = 5$ mm at its left end. The fin is uniformly subjected to a normal load $P = -2$ bar on its upper surface and is fully constrained at its left end, as illustrated in Figure 14.

The fin is made of steel with $E = 200$ GPa and $\nu = 0.3$, and follows a plane stress state.

The classical problem of an infinite elastic wedge, solved by Timoshenko [41, 24], serves as the benchmark solution. This problem is modeled in a polar coordinate system (r, θ) , where $r = 0$ is located at the apex of the wedge. The angle θ ranges from 0 to β , with $\beta = 0.05$ rad being the wedge angle. The upper surface of the wedge is loaded at $\theta = 0$, as illustrated in Figure 15.

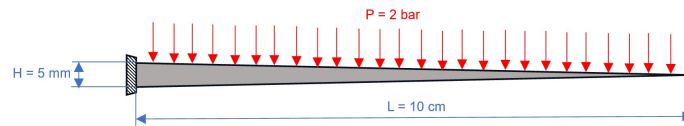


Figure 14: Very thin fin subjected to a bending effort

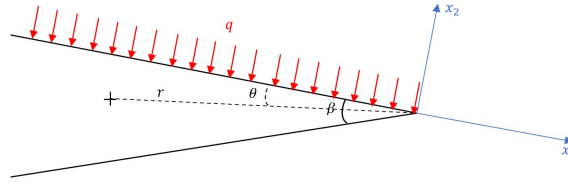


Figure 15: Model of an infinite elastic wedge subjected to a uniform pressure on its upper surface

According to [41, 24], the stress components depend only on θ and are given by

$$\begin{cases} \sigma_{rr}(\theta) = \frac{q}{k} \left(-k + \frac{1}{2} \tan \beta - \theta + \frac{1}{2} \tan \beta \cos 2\theta - \frac{1}{2} \sin 2\theta \right), \\ \sigma_{\theta\theta}(\theta) = \frac{q}{k} \left(-k + \frac{1}{2} \tan \beta - \theta - \frac{1}{2} \tan \beta \cos 2\theta + \frac{1}{2} \sin 2\theta \right), \\ \sigma_{r\theta}(\theta) = \frac{q}{2k} (1 - \tan \beta \sin 2\theta - \cos 2\theta), \end{cases} \quad (28)$$

where $k = \tan \beta - \beta$. The displacement field is obtained by integrating the strains, which are derived from the linear-elastic constitutive law (Hooke's law), while satisfying the compatibility equations. The resulting integration constants are determined by imposing displacement boundary conditions at $r = L$ (L being the length of the fin), as follows:

$$\begin{cases} u_r(L, 0) = u_r\left(L, \frac{\beta}{2}\right) = 0, \\ u_\theta\left(L, \frac{\beta}{2}\right) = 0. \end{cases} \quad (29)$$

The resulting displacement field is

$$\begin{cases} u_r(r, \theta) = \frac{q}{Ek} \left[(1 - \nu) \left(\frac{1}{2} \tan \beta - (k + \theta) \right) + (1 + \nu) \frac{\sin(\beta - 2\theta)}{2 \cos \beta} \right] r \\ \quad + C_1 \cos \theta + C_2 \sin \theta, \\ u_\theta(r, \theta) = \frac{q}{Ek} \left[2 \log \frac{r}{L} + \frac{1 + \nu}{2 \cos \beta} (1 - \cos(\beta - 2\theta)) \right] r \\ \quad + C_1 \left(\sin \left(\frac{\beta}{2} \right) \frac{r}{L} - \sin \theta \right) + C_2 \left(\cos \theta - \cos \left(\frac{\beta}{2} \right) \frac{r}{L} \right), \end{cases} \quad (30)$$

with the constants C_1 and C_2 given by

$$\begin{cases} C_1 = \frac{qL}{Ek} ((1-\nu)k - \tan \beta), \\ C_2 = \frac{qL}{Ek} \left(\frac{\tan \beta}{\tan \frac{\beta}{2}} + (1-\nu)k \frac{1 - 2 \cos \frac{\beta}{2}}{2 \sin \frac{\beta}{2}} \right). \end{cases} \quad (31)$$

To perform the computational tasks, a BEM code was developed, using the C++ programming language. The problem is then solved using this code, employing both existing integration criteria and the newly proposed criterion.

The analytically obtained results for the infinite wedge should align with the numerical results except at locations near the fixed base, where the resulting errors are not accounted for in the evaluation of the different criteria. More specifically, the obtained results confirmed that the analytical solution aligns well with the numerical results at $x > 3cm$.

The relative errors are evaluated by

$$\epsilon = \left| \frac{Res_{analytical} - Res_{BEM}}{Res_{analytical}} \right|. \quad (32)$$

The effectiveness of the proposed criterion is assessed across various values of α aiming for a target precision of 10^{-3} .

4.1 The displacement solution

To analyze the displacement solution, a series of 40 probe points are placed along the horizontal direction of the fin at $\theta = \frac{\beta}{2}$. The displacement magnitude $U = \sqrt{U_1^2 + U_2^2}$ is evaluated at each point within this set.

The curves presented in Figure 16 illustrate the variation of the displacement magnitude along the length of the fin. Whereas, Figure 17 illustrates the variation of the relative error versus the horizontal location. Upon analysis of the results depicted in Figure 16, a notable correspondence between the displacement magnitudes obtained from the analytical solution and the numerical (BEM) solutions when employing the criterion of Junhao and the new criterion with α values of 0.8 and 1 is observed. However, utilizing

the remaining existing criteria (Lachat and Watson, Jun and Beer, Gao and Davies and Eberwien) or the new criterion with low α values leads to fluctuating results, particularly near the fin tip, resulting in higher errors.

Additionally, Figure 17 illustrates how the relative error tends to escalate in thinner regions when employing either existing criteria or the new criterion with lower α values. However, when using the new integration criterion with α values close to 1, the error begins to decrease and remains relatively stable, even in extremely thin regions. Specifically, for $\alpha = 1$, the error decreased slightly below the target error upper bound of 10^{-3} . Moreover, although the Junhao criterion produced acceptable and good quality results, the resulting relative error remained above the required upper bound. In contrast, the new criterion yielded better results even with $\alpha = 0.8$, with a net gain in efficiency as stated previously in section 3.6 and illustrated in Figure 13, where the new criterion's curves are situated below Junhao's curve in the case of moderate values of the λ ratio. Furthermore, this favored interval grows wider as α is decreased. As, for $\alpha = 0.8$, this interval becomes $[0.000381564, 2.09121]$. Based on the preceding analysis, the new criterion demonstrated a high level of accuracy in displacement results, offering improved and more consistent precision, even in regions of extreme thinness. In contrast, the existing criteria were unable to satisfy the required upper error bound, largely due to the strong influence of boundary layer effect, especially in the thinner sections of the fin.

4.2 The stress solution

4.2.1 Stress assessment in the horizontal direction

In contrast to the displacements, which exhibit significant variations along the horizontal direction, the major stress variations occur along the vertical direction of the fin, as it is confirmed by the stress analytical solution of the infinite wedge problem, which varies only in terms of θ (see (28)). Consequently, the previously utilized probe points are not used for stress assessment. Given that stress reaches its maximum values at the boundary

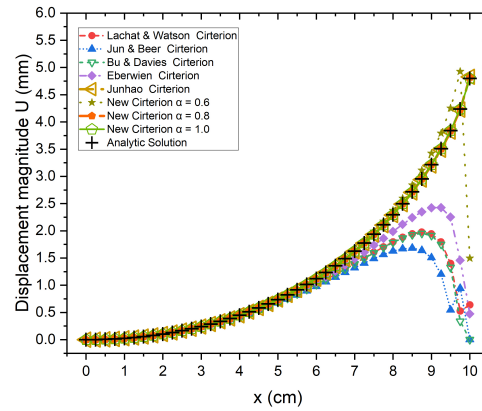


Figure 16: Variation of the displacement magnitude along the horizontal direction of the fin

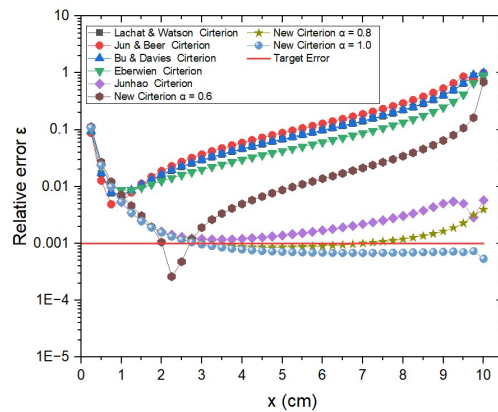


Figure 17: The variation of the relative error for displacement magnitude along the horizontal direction of the fin

of the fin, the initial analysis of the stress solution involves probing 40 points positioned on the top side of the fin.

The curves in Figure 18 illustrate the variation of von Mises equivalent stress along the upper surface of the fin. Whereas, Figure 19 depicts the variation of the corresponding relative error with respect to the horizontal location.

A detailed examination of the curves in Figure 18 reveals significant fluctuations and the presence of very important errors in stress solution, particularly

when utilizing existing criteria or the new criterion with relatively low values for the α coefficient. These fluctuations and errors increase drastically as the fin tip is approached. Notably, these errors are more pronounced compared to the displacement solution, attributable to the higher singularity order $O\left(\frac{1}{r^2}\right)$ of the kernels employed in the stress solution.

However, with the adoption of the Junhao criterion and the new integration criterion using α values of 0.8 and 1, satisfactory results are obtained, even in extremely thin sections very close to the fin tip, without necessitating any analytical or semi-analytical treatment.

Figure 19 depicts, akin to Figure 17, the significant increase of errors in thinner regions, with values reaching approximately a twenty (20) times higher than displacement errors in some cases. Nonetheless, the proposed criterion with $\alpha = 1$ yields acceptable errors, below the target upper bound of 10^{-3} . Moreover, although the Junhao criterion produced acceptable and good quality results, the resulting relative error remained above the required upper bound. While, the proposed criterion yielded better results even with $\alpha = 0.8$. and remain stable even in thinner sections, with a gain in efficiency, as seen in section 4.1.

From the results above, it is evident that the new criterion was capable of producing very accurate results in stress response, with improved and more stable precision in regions of extreme thinness, despite the augmented order of the near-singularities appearing in stress kernel functions. In contrast, the existing criteria resulted in excessively high errors, exceeding those reported in section 4.1 by approximately a factor of twenty.

4.2.2 Stress assessment in the vertical direction

To further assess the stress solution, especially the variation in terms of θ , three cross sections are considered, having these respective distances from the apex $\{r = 50 \text{ mm}, 20 \text{ mm}, 5 \text{ mm}\}$ corresponding to $\{x = 5 \text{ cm}, 8 \text{ cm}, 9.5 \text{ cm}\}$, respectively.

The three graphs in Figures 20, 21, and 22 illustrate the variation of the relative errors for the Von-Mises stress along these 3 delineated sections.

Upon comparing the results presented in Figures 20–22, it is evident that the

von Mises stress computed using the various existing criteria (Lachat and Watson, Jun and Beer, Bu and Davies, and Eberwien) exhibits significantly high errors, all exceeding the required upper bound. These errors become more pronounced near the boundaries, specifically at $\theta \approx 0$ and $\theta \approx \beta = 0.05$ rad, as clearly illustrated in Figures 20–22 when approaching the left and right ends.

Furthermore, these errors increase drastically as the cross-section approaches the apex. Thus, errors illustrated in Figure 22 at $r = 5$ mm are the most pronounced.

Nevertheless, by using our new integration criterion with $\alpha = 1$, we obtained a highly stable precision that meets the target upper bound of $\epsilon = 10^{-3}$, even in the extremely thin cross section at $r = 5$ mm and at points very close to the boundary ($\theta \approx 0$ and $\theta \approx \beta = 0.05$ rad).

Once again, the proposed criterion demonstrated its ability to accurately represent the stress field distribution, even in extremely thin cross-sections and at points very close to the boundary, while maintaining a highly stable relative error with respect to the imposed error threshold.

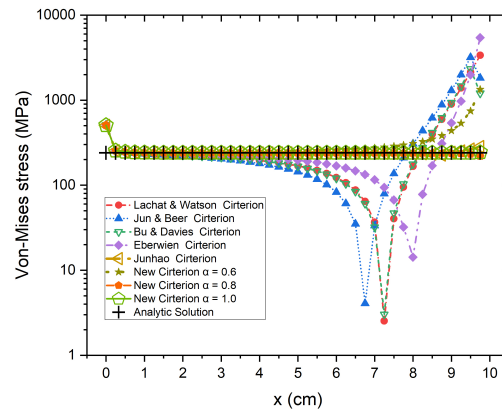


Figure 18: Variation of the von Mises equivalent stress along the fin

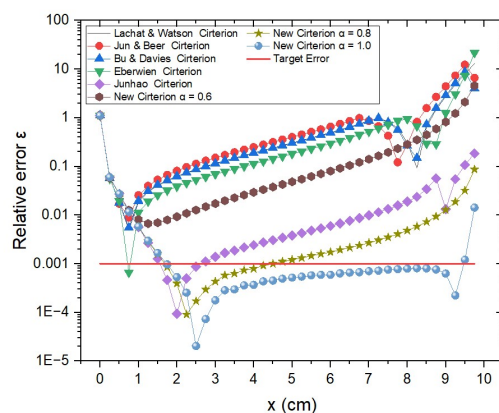


Figure 19: The variation of the relative error of von Mises stress along the horizontal direction of the fin

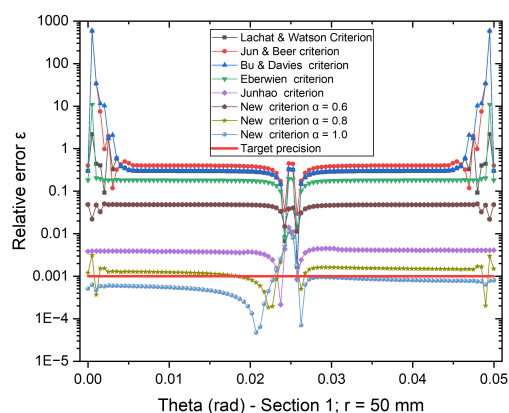


Figure 20: Relative error for the von Mises stress in terms of θ across the the section at ($r=50$ mm)

4.3 Further computational improvement

As stated in the introduction, analytical and semi-analytical techniques, particularly nonlinear variable transformations, are employed to treat near-singularities. Most of these methods aim to mitigate or eliminate the effects of near singularities, resulting in a less pronounced singular behavior. How-

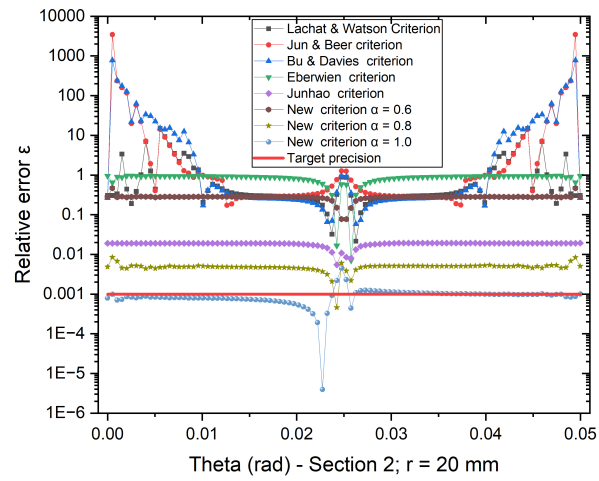


Figure 21: Relative error for the von Mises stress in terms of θ across the the section at ($r=20$ mm)

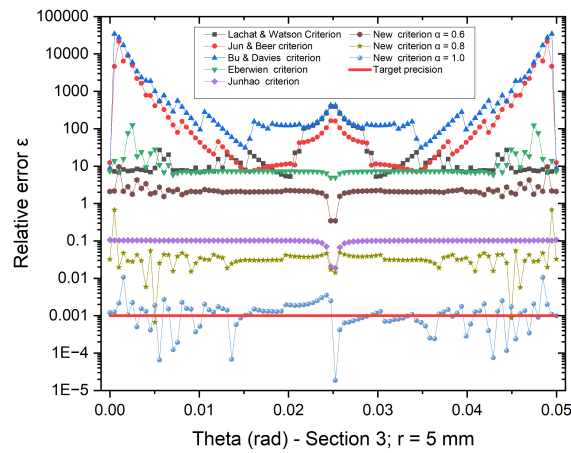


Figure 22: Relative error for the von Mises stress in terms of θ across the the section at ($r=5$ mm)

ever, in the case of very thin bodies, despite reducing the boundary layer effect, its influence remains significant.

This will be demonstrated in the current section using the sinh variable transformation technique in combination with different integration criteria to solve the previously discussed example. One of the major advantages of the proposed criterion will also be illustrated, namely, its ability to reduce computational effort by lowering the parameter α , taking advantage of the dampened singularity.

The same 40 probe points used in sections 4.1 and 4.2.1 are employed here to evaluate the displacement magnitude and Von Mises stress, respectively. The results are presented in Figures 23 and 24, showing the relative error of both quantities.

Figures 23 and 24 reveal that, despite applying the sinh transformation, the existing criteria (Lachat and Watson, Jun and Beer, Gao and Davies, and Eberwien) still yield poor accuracy, with relative errors exceeding the desired error threshold.

In contrast, the proposed criterion combined with the sinh transformation and a reduced value of $\alpha = 0.6$ delivers excellent results, comparable to those obtained with $\alpha = 1$ without variable transformation.

The combination of the Junhao criterion and the sinh transformation also produced acceptable accuracy, though not as high as that achieved by the proposed criterion.

Furthermore, as discussed in section 3.6 and shown in the log-log plot of Figure 13, the Junhao criterion's error upper-bound formula leads to more Gauss points for moderate values of λ . In this case, with $\alpha = 0.6$, the interval over which the proposed criterion outperforms the Junhao criterion is wider than when $\alpha = 1$, becoming $\lambda \in [2.36258 \times 10^{-5}, 3.19886]$.

In conclusion, the application of the sinh variable transformation allowed further computational improvement with accurate results that satisfy the prescribed precision requirements while reducing computational cost through lower values of α . Additionally, in the case of extremely thin structures, although the combination of existing criteria with the sinh transformation showed some improvement, the results remained unsatisfactory, with relative errors still exceeding the required precision threshold.

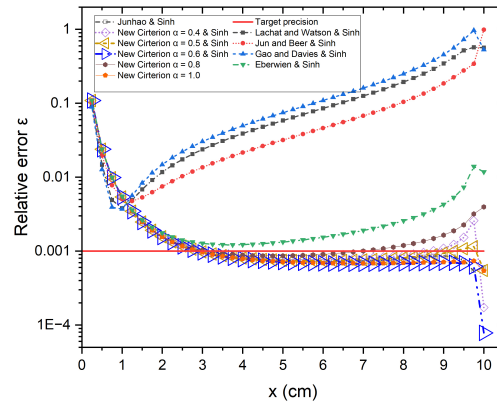


Figure 23: Relative error for the displacement magnitude when utilizing the sinh variable transformation

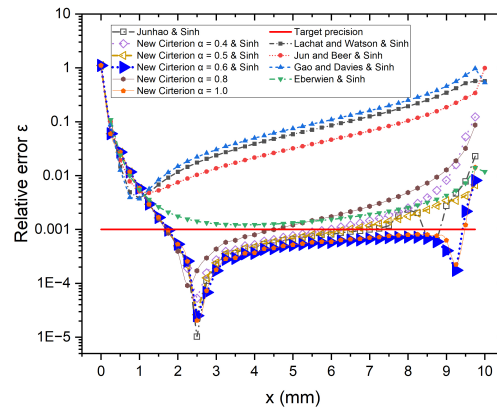


Figure 24: Relative error for the von Mises stress when utilizing the sinh variable transformation

5 Conclusion

The utilization of Gaussian quadrature for numerical integration within the BEM is practically indispensable. Consequently, the choice of quadrature order significantly impacts the accuracy and efficiency of computational codes and programs based on this method. Various criteria and error bound for-

mulas existing in BEM literature, were used for the purpose of an optimal selection of the Gauss order. The majority of these criteria and upper bound error formulas were developed under the assumption of a simplified form for the integration kernels.

In order to develop a criterion that meets high precision requirements in extremely thin bodies, a numerical testing procedure was performed to estimate the errors due to numerical integration using Gauss-Legendre quadrature, but in contrast to previous research works the complete form of the integrands is considered. From the numerically obtained results, a new integration criterion is proposed, formulated as empirical formulas with a unified structure incorporating a parameter named α . This parameter facilitates the adjustment of computational efforts, by enabling its reduction in case of nonthin bodies or after the use of semi-analytical algorithms and variable transformation techniques. Simulations are conducted on an extremely thin structure (a thin wedge), and the results are compared to the analytical solution for an infinite wedge. The comparison showed that results align well at locations relatively far from the fixed base and demonstrated the criterion's ability to achieve highly accurate results. For the optimal parameter value $\alpha = 1$, the proposed criterion outperformed existing criteria, delivering results with stable precision that satisfied the upper bound error requirement of $\epsilon = 10^{-3}$, even in regions close to the wedge apex. Furthermore, the proposed criterion showed its advantage in controlling computational efforts, which is demonstrated through the application of the sinh transformation technique, where additional computational time is reduced by lowering the value of α to 0.6.

Acknowledgements

The support from Directorate-General for Scientific Research and Technological Development (DG-RSDT) of Algerian government in the form of research grant is gratefully acknowledged. The Laboratory of Green and Mechanical Development (LGMD) of National Polytechnic School (ENP) is also gratefully acknowledged for the resources and support.

References

- [1] Aliabadi, M.H., *The boundary element method – applications in solids and structures*, Wiley, Volume 2. UK, Chichester, 2002.
- [2] Aliabadi, M.H., Hall, W.S., and Phemister, T.G., *Taylor expansions for singular kernels in the boundary element method*, Int. J. Numer. Methods Eng. 21 (1985), 2221–2236.
- [3] Araújo, F.C., and Gray, L.J., *Analysis of thin-walled structural elements via 3D standard BEM with generic substructuring*, Comput. Mech. 41 (2008), 633–645.
- [4] Bu, S., and Davies, T.G., *Effective evaluation of non-singular integrals in 3D BEM*, Adv. Eng. Softw. 23 (2) (1995), 121–128.
- [5] Chang, C., and Mear, M.E., *A boundary element method for two-dimensional linear elastic fracture analysis*, Int. J. Fract. 74 (1995), 219–25.
- [6] Chen, H.B., Lu, P., Huang, M.G., and Williams, F.W., *An effective method for finding values on and near boundaries in the elastic BEM*, Comput. Struct. 69 (1998), 421–431.
- [7] Chen, H.B., Lu, P., and Schnack, E., *Regularized algorithms for the calculation of values on and near boundaries in 2D elastic BEM*, Eng. Anal. Bound. Elem. 25 (10) (2001), 851–876.
- [8] Chernov, A., and Stephan, E.P., *Adaptive BEM for Contact Problems with Friction*, Peter Wriggers and Udo Nackenhorst (eds.), In IUTAM Symposium on Computational Methods in Contact Mechanics: Proceedings of the IUTAM Symposium held in Hannover, Germany, November 5–8, 2006, pp. 113–122. Dordrecht: Springer Netherlands, 2007.
- [9] Cruse, T.A., and Aithal, R., *Non-singular boundary integral equation implementation*, Int. J. Numer. Method. Eng. 36 (1993), 237–254.
- [10] Eberwien, U., Duencer, C., and Moser, W., *Efficient calculation of internal results in 2D BEM*, Eng. Anal. Bound. Elem. 29 (2005), 447–453.

- [11] Gao, X.W., and Davies, T.G., *Adaptive integration in elasto-plastic boundary element analysis*, J. Chin. Inst. Eng. 23 (3) (2000), 349–356.
- [12] Gu, Y., Chen, W., and Zhang, C., *Stress analysis for thin multilayered coating systems using a sinh transformed boundary element method*, Int. J. Solids Struct. 50 (20-21) (2013), 3460–3471.
- [13] Gu, Y., Zhang, C., Qu, W., and Ding, J., *Investigation on near-boundary solutions for three-dimensional elasticity problems by an advanced BEM*, Int. J. Mech. Sci. 142–143 (2018), 269–275.
- [14] Guiggiani, M., *Hypersingular formulation for boundary stress evaluation*, Eng. Anal. Bound. Elem. 13 (1994), 169–179.
- [15] Guiggiani, M., *The evaluation of Cauchy principal value integrals in the boundary element method – A review*, Math. Comput. Model. 15(3-5) (1991), 175–184.
- [16] Guiggiani, M., and Casalini, P., *Direct computation of Cauchy principal value integrals in advanced boundary elements*, Int. J. Numer. Methods Eng. 24 (1987), 1711–1720.
- [17] Guiggiani, M., and Casalini, P., *Rigid body translation with curved boundary elements*, Appl. Math. Model. 13(6) (1989), 365–368.
- [18] Gwinner, J. and Stephan, E.P., *A boundary element procedure for contact problems in plane linear elastostatics*, ESAIM: Math. Model. Numer. Anal. 27 (4) (1994), 457–480.
- [19] Jing, R., Yu, B., Ren, S., and Yao, W., *A novel SCTBEM with inversion-free Padé series expansion for 3D transient heat transfer analysis in FGMs*, Comput. Method. Appl. Mech. Eng. 433 (2025), 117546.
- [20] Johnston, P.R., and Elliott, D., *Transformations for evaluating singular boundary element integrals*, J. Comput. Appl. Math. 146 (2) (2002), 231–251.
- [21] Johnston, P.R., and Elliott, D., *A sinh transformation for evaluating nearly singular boundary element integrals*, Int. J. Numer. Method. Eng. 62 (2005), 564–578.

- [22] Jun, L., Beer, G., and Meek, J.L., *Efficient evaluation of integrals of order $1/r$, $1/r^2$, $1/r^3$ using Gauss quadrature*, Eng. Anal. 2 (3) (1985), 118–123.
- [23] Junhao, H., Zhipeng, W., and Yongqiang, C., *A new error upper bound formula for Gaussian integration in boundary integral equations*, Eng. Anal. Bound. Elem. 112 (2020), 39–45.
- [24] Kachanov, M., Shafiro, B., and Tsukrov, I., *Handbook of elasticity solutions*, Springer Science+Business Media Dordrecht, B.V, 2003.
- [25] Lachat, J.C., and Watson, J.O., *Effective numerical treatment of boundary integral equations: A formulation for three dimensional elastostatics*, Int. J. Numer. Method. Eng. 10 (1976), 991–1005.
- [26] Li, S., and Mear, M.E., *Singularity-reduced integral equations for displacement discontinuities in three-dimensional linear elastic media*, Int. J. Fract. 93 (1998), 87–114.
- [27] Ma, H., and Kamiya, N., *Distance transformation for the numerical evaluation of near singular boundary integrals with various kernels in boundary element method*, Eng. Anal. Bound. Elem. 26 (2002), 329–339.
- [28] Mi, Y., and Aliabadi, M.H., *A Taylor expansion algorithm for integration of 3D near-singular integrals*, Commun. Appl. Numer. Method. Eng. 12 (1996), 51–62.
- [29] Mustoe, G.G.W., *Advanced integration schemes over boundary elements and volume cells for two-and three-dimensional non-linear analysis*, Develop. Bound. Elem. Method. 3 (1984), 213–270.
- [30] Newman-Jr, J.C., Mear, J.M., and Raju, I.S., *Computer simulation of elastic stress analyses of two-dimensional multiple-cracked bodies*, 37th Structure, Structural Dynamics and Materials Conference, AIAA Meeting Papers on Disc 1996, 869–876.
- [31] Padhi, G.S., Shenoi, R.A., Moy, S.S.J., and McCarthy, M.A., *Analytic integration of kernel shape function product integrals in the boundary element method*, Comput. Struct. 79 (14) (2001), 1325–1333.

- [32] Paulsen, K.D., and Lynch, D.R., *Calculation of interior values by the boundary element method*, Commun. Appl. Numer. Method. 5 (1989), 7–14.
- [33] Portella, A., Aliabadi, M.H., and Rooke, D.P., *The dual boundary element method: effective implementation for crack problems*, Int. J. Numer. Method. Eng. 33 (1992), 1269–1287.
- [34] Portella, A., Aliabadi, M.H., and Rooke, D.P., *Dual boundary element incremental analysis of crack propagation*, Comput. Struct. 46 (02) (1993), 237–247.
- [35] Rudolphi, T.J., *The use of simple solutions in the regularization of hypersingular boundary integral equations*, Math. Comput. Model. 15 (3–5) (1991), 269–278.
- [36] Salvadori, A., *Analytical integrations in 2D BEM elasticity*, Int. J. Numer. Method. Eng. 53 (2002), 1695–1719.
- [37] Sladek, V., Sladek, J., and Tanaka, M., *Nonsingular BEM formulations for thin-walled structures and elastostatic crack problems*, Acta Mech. 99 (1993), 173–190.
- [38] Sladek, V., Sladek, J., and Tanaka, M., *Optimal transformations of the integration variables in computation of singular integrals in BEM*, Int. J. Numer. Method. Eng. 47 (2000), 1263–1283.
- [39] Stroud, A.H., and Secrest, D., *Gaussian quadrature formulas*, Prentice-Hall Inc, Englewood Cliffs, N.J. 1966.
- [40] Telles, J.C.F., *A self-adaptive coordinate transformation for efficient numerical evaluation of general boundary element integrals*, Int. J. Numer. Method. Eng. 24 (1987), 959–973.
- [41] Timoshenko, S., and Goodier, J.N., *Theory of elasticity*, McGraw-Hill book company, New York, 1951.
- [42] Yu, B., and Jing, R., *SCTBEM: A scaled coordinate transformation boundary element method with 99-line MATLAB code for solving Poisson's equation*, Comput. Phys. Commun. 300 (2024), 109185.

- [43] Zhang, X. and Zhang, X. *Exact integration in the boundary element method for two-dimensional elastostatic problems*, Eng. Anal. Bound. Elem. 27 (2003), 987–997.
- [44] Zhang, X. and Zhang, X. *Exact integration for stress evaluation in the boundary element analysis of two-dimensional elastostatics*, Eng. Anal. Bound. Elem. 28 (2004), 997–1004.
- [45] Zhang, Y., Gong, Y., and Gao, X., *Calculation of 2D nearly singular integrals over high-order geometry elements using the sinh transformation*, Eng. Anal. Bound. Elem. 60 (2015), 144–153.
- [46] Zhang, Y., and Gu, Y., *An effective method in BEM for potential problems of thin bodies*, J. Mar. Sci. Technol. 18 (2010), 137–144.
- [47] Zhang, Y., Gu, Y., and Chen, J.T., *Analysis of 2D thin-walled structures in BEM with high-order geometry elements using exact integration*, Comput. Model. Eng. Sci. 50 (2009), 1–20.
- [48] Zhou, W., Yang, X., and Chen, Y., *Adaptive sinh transformation Gaussian quadrature for 2D potential problems using deep learning*, Eng. Anal. Bound. Elem. 155 (2023), 197–211.